NASA TM-86011

NASA Technical Memorandum 86011

NASA-TM-86011 19850004008

Numerical Studies of Unsteady Transonic Flow over an Oscillating Airfoil

W.J. Chyu and S.S. Davis

October 1984

LIBRARY COPY

LANGLEY RESEARCH CENTER
LIBRARY
HAMPTON, VIRGINIA

National Aeronautics and
Space Administration

NF00856

NASA Technical Memoradum 86011

Numerical Studies of Unsteady Transonic Flow over an Oscillating Airfoil

W. J. Chyu,
S. S. Davis, Ames Research Center, Moffett Field, California

National Aeronautics and
Space Administration

Ames Research Center
Moffett Field, California 94035

NUMERICAL STUDIES OF UNSTEADY TRANSONIC FLOW OVER AN OSCILLATING AIRFOIL

W J Chyu and S S Davis
NASA Ames Research Center, Moffett Field, California 94035, U.S.A.

SUMMARY

A finite-difference solution to the Navier-Stokes equations combined with a time-varying grid-generation technique was used to compute unsteady transonic flow over an oscillating airfoil. These computations were compared with experimental data (obtained at Ames Research Center) which form part of the AGARD standard configuration for aeroelastic analysis A variety of approximations to the full Navier-Stokes equations was used to determine the effect of frequency, shock-wave motion, flow separation, and airfoil geometry on unsteady pressures and overall air loads Good agreement is shown between experiment and theory with the limiting factor being the lack of a reliable turbulence model for high-Reynolds-number, unsteady transonic flows.

SYMBOLS

a	speed of sound
c	chord length
c_p	specific heat at constant pressure
C_p	pressure coefficient normalized by $\rho_\infty a_\infty^2$
$C^n_{p,\alpha}$	nth complex component of C_p per radian of α
e	total energy per unit volume normalized by $\rho_\infty a_\infty^2$
J	Jacobian of transformation between physical and computational coordinates, $J = (\xi_x \eta_y - \xi_y \eta_x)$
k	reduced frequency, $\omega c/2U_\infty$
M	Mach number
p	pressure, normalized by $\rho_\infty a_\infty^2$
Pr	Prandtl number, $\mu c_p/\kappa^*$
Re	Reynolds number, $\rho_\infty a_\infty c/\mu_\infty$
u,v	Cartesian velocities, normalized by a_∞
U_∞	free-stream velocity
x,y	physical Cartesian coordinates, normalized by c
α	angle of attack
$\tilde{\alpha}$	amplitude of airfoil oscillation
γ	ratio of specific heats
κ	coefficient of thermal conductivity, normalized by κ^*
ξ,η	computational coordinates in streamwise and normal spatial directions
ρ	density normalized by ρ_∞
μ,λ	first and second viscosity normalized by μ^*
τ	time variable, $\tau = ta_\infty/c$
$\tau_{xx},\tau_{yy},\tau_{xy}$	skin friction

Subscripts

∞	free-stream value
m	mean value

Superscripts

$*$	reference value

INTRODUCTION

The proper computation of unsteady, transonic viscous flows around an oscillating airfoil remains an outstanding and important problem in fluid dynamics An efficient and complete analytical capability to predict the flow would find immediate applications in the treatment of aeroelastic (flutter and buffet) and control-response analyses for both fixed- and rotary-wing aircraft. The theoretical analysis of transonic flows is complicated by the presence of mixed subsonic and supersonic regions within the flow field For the unsteady flow field, such as that surrounding an oscillating airfoil, additional considerations are needed to treat time-dependent aerodynamic loads caused by moving shock waves and boundary-layer interactions At Ames Research Center, studies related to these problems have been conducted in recent years, both theoretically and experimentally, to predict and clarify many aspects of these flows.

The physics of unsteady, transonic flow can be simulated at various levels of inviscid and viscous approximations For those cases in which viscous effects dominate, computations based on the Navier-Stokes equations are needed. Beam and Warming (Ref 1) report on an efficient implicit numerical algorithm for compressible viscous flow in which an implicit factorization scheme is used Steger (Ref 2) applied this technique to the unsteady, compressible Navier-Stokes equations, using the thin-layer approximation In Ref 3 he numerically demonstrated the dynamic phenomena of transonic buffet and aileron buzz Recently, Chyu et al (Refs 4-7) applied a related numerical method for analyzing unsteady, transonic flows over an oscillating airfoil, the method combined the numerical technique reported by Steger with a new and efficient time-varying, grid-generation technique suitable for the treatment of moving airfoils. The method was recently applied by Horiuti et al (Ref. 8) to the analysis of transonic flows over an airfoil with oscillating flap

The purpose of this paper is to summarize the results of a 6-year effort in the Ames Aerodynamics Research Branch to measure and calculate unsteady transonic flows By using certain data sets identified by AGARD as a standard configuration (Ref 9), a series of increasingly complicated unsteady transonic flow cases will be analyzed The effects of frequency, flow separation, and airfoil geometry will be studied, and it will be shown that increasingly complex flows demand increasingly sophisticated equations to correctly model the flow

N85-12316 #

pattern. The computed results presented here also show that the differences between the full and thin-layer Navier-Stokes equations are not significant for this class of flows.

NUMERICAL PROCEDURE

A numerical procedure is briefly described for computing the unsteady flow field induced by an oscillating airfoil in transonic flow The development of the equations, finite-difference algorithm, boundary treatment, and grid system follows closely that developed in Refs. 1, 2, and 6.

Governing Equations

An implicit finite-difference scheme was used to solve the full time-dependent compressible Navier-Stokes equations in conservation-law form. The numerical algorithm adopted for this study is the Beam-Warming spatially factored scheme. The application of the algorithm to the Navier-Stokes equations subject to the general transformation, $\xi = \xi(x,y,t)$, $\eta = \eta(x,y,t)$, $\tau = t$ (Fig 1) is present in the Appendix

For turbulent flows, the viscosity coefficient is computed using the two-layer, Cebeci-type eddy-viscosity model reported by Baldwin and Lomax (Ref 10). The main features of the Baldwin-Lomax model are the determination of the eddy mixing-length scale based on the local vorticity In the present work, the instantaneous vorticity is calculated after each time-step of computation

Boundary Conditions

On the outer boundary of the grids, free-stream conditions were applied On the airfoil surface, the Cartesian velocities are

$$\begin{pmatrix} u \\ v \end{pmatrix} = J^{-1} \begin{bmatrix} \eta_y & -\xi_y \\ -\eta_x & \xi_x \end{bmatrix} \begin{bmatrix} U - \xi_t \\ V - \eta_t \end{bmatrix}$$

where the contravariant velocity components U and V are defined as

$$U = \xi_t + \xi_x u + \xi_y v \ , \qquad V = \eta_t + \eta_x u + \eta_y v$$

and

$$\xi_t = -x_\tau \xi_x - y_\tau \xi_y \ , \qquad \eta_t = -x_\tau \eta_x - y_\tau \eta_y$$

with x_τ and y_τ determined from local airfoil surface velocities For viscous flow, the no-slip condition requires that $U = V = 0$ at the airfoil surface

For inviscid computations, a tangency condition is imposed on the airfoil surface by setting V to zero, and U is determined at the body surface by a linear extrapolation from the flow field determined at the previous step. At the trailing edge of the airfoil, the Cartesian velocities u and v are set equal to x_τ and y_τ, respectively, to satisfy the Kutta condition. The surface pressure is determined from the normal momentum equation in both the inviscid and viscous computations

Grid Generation

Stationary grids were first constructed for the airfoil at its extreme angle-of-attack positions Grids at intermediate angles of attack were obtained from those at the extreme positions by spatial interpolation The extreme-position grids were generated by numerical solutions of elliptic equations (Refs 4 and 11) This technique permits grid points to be specified along the entire boundary of the computational plane In Fig 1, the boundary is indicated by a curve a-b-c-d-e-f-g-h-i-a in a physical plane that encompasses the airfoil, wake, and far-field Application of the method then generates a smoothly spaced, non-overlapping grid at the interior points.

In the present work, boundary points were specified at fixed locations along the airfoil, with grid spacing clustered near the leading and trailing edges of the airfoil and near the shock-wave position. The grid points on the wake (a line, ab or de, in Fig 1) were chosen to lie on a third-degree polynomial arc tangent to the bisector of airfoil at its trailing edge and returning to the airfoil centerline at the downstream outer boundary This procedure aligns the grid points in the wake with the approximate initial and final directions of the wake flow (Fig 2), which was found to improve the efficiency of the flow-field computations. Finally, grid points at the free-stream boundary are chosen to lie approximately 8 chord lengths above and below the airfoil and 8 chords upstream and downstream of the airfoil leading edge. The outer boundary points remain fixed in space for all angles of attack This general approach of fixing the outer boundary points permits treating an airfoil oscillating in the proximity of a wall, a second airfoil, or a flap oscillating behind a fixed airfoil, as was done in Ref 8.

Once the grid is specified on its boundaries, an elliptic solver is used to generate a smoothly spaced grid at the interior points This grid is then re-spaced, or clustered, along ξ = const lines (lines moving away from the airfoil), using the weighted coordinate-stretching technique advocated in Ref. 4

Allowing the airfoil surface to vary within a stationary outer boundary requires that a new grid be generated at each time-step of the computation To reduce the computational effort needed to repeatedly generate the grid, a novel grid interpolation scheme was devised (Ref. 4). Grids were generated at the extreme angle-of-attack positions of the prescribed airfoil motion, using the elliptic equation and the weighted coordinate-stretching techniques described previously, these grids were then stored. Grids needed at intermediate airfoil patterns were found from interpolation along the circular arcs that were assumed to represent the locus of the grid-point movement The radius of curvature for each point of the grid was taken as the

distance between the grid point and the fixed pivot point about which the airfoil was oscillating. With the radius of curvature and the extreme positions known, the center of curvature was then computed for each grid point. Grid points for intermediate values of the angle of attack were found from a linear interpolation of arc length along the curves defined in this manner. This method of grid interpolation eliminated entanglement of coordinate lines during the airfoil motion, even within the dense grids in the boundary-layer region. An example of the grid patterns generated by this interpolation method is shown in Fig. 2. Grids similar to those used in computations obtained at the extreme angle-of-attack positions are shown in Figs. 2(a) and 2(b), and an interpolated grid is shown in Fig 2(c).

Complex Representation of Surface-Pressure Variation

The time variation of the surface-pressure distributions is expressed in terms of its Fourier components. The harmonically varying angle of attack can be expressed as

$$\alpha(t) = \alpha_m + \mathrm{Re}(\tilde{\alpha}\, e^{i\omega t})$$

where Re represents the real part of the complex argument. The Fourier series representation of the surface-pressure coefficient is

$$C_p(x/c,t) = C_{p_m}(x/c) + \sum_{n=1}^{\infty} \mathrm{Re}[C^n_{p,\tilde{\alpha}}(x/c)\tilde{\alpha}\, e^{in\omega t}]$$

where $C_{p_m}(x/c)$ is the mean value of the local surface-pressure coefficient and $[C^n_{p,\tilde{\alpha}}(x/c)]$ is the nth complex component of the local unsteady pressure coefficient, per radian The real and imaginary value of $C_{p,\tilde{\alpha}}$ can be expressed as

$$\mathrm{Re}[C^n_{p,\tilde{\alpha}}(x/c)] = (C^n_p/\tilde{\alpha})\cos\phi_n$$

and

$$\mathrm{Im}[C^n_{p,\tilde{\alpha}}(x/c)] = (C^n_p/\tilde{\alpha})\sin\phi_n$$

where C^n_p is the nth harmonic unsteady pressure (real) and ϕ_n is the nth harmonic phase shift between the angle of attack and the pressure response.

RESULTS

Experimental Measurements

A series of experimental measurements has been carried out in the 11- by 11-Foot Transonic Wind Tunnel at Ames Research Center. In these experiments, a NACA 64A010 airfoil and an NLR 7301 airfoil underwent small-amplitude harmonic oscillations in pitch about various pivot axes located along the airfoil chord (Refs. 9 and 12-17) The test Mach numbers ranged from 0.5 to 0.8, chord Reynolds numbers from $2\ 5 \times 10^6$ to $12\ 5 \times 10^6$ were obtained. Unsteady pressure distributions were measured on the airfoil during the course of the oscillations, and unsteady aerodynamic forces and moments were obtained subsequently from integration of the pressure distributions. The cases of interest for the present study of the NACA 64A010 airfoil had the airfoil oscillating about a pivot at $x/c = 0\ 25$, with an amplitude of oscillation, $\tilde{\alpha} = 1°$, and a mean value of the pitch angle $\alpha_m = 0°$ and $4°$ (With the pitching axes fixed, the pitch angle is equivalent to the instantaneous angle of attack of the airfoil) The range of reduced frequency of the oscillation, k, was taken from 0.025 to 0 20, and the Mach and Reynolds numbers were held fixed at $M_\infty = 0\ 8$ and $Re = 12 \times 10^6$, respectively (Table 1).

For the NLR 7301 supercritical airfoil, the airfoil was caused to oscillate in pitch about a pivot at $x/c = 0\ 4$, with an amplitude of oscillation $\tilde{\alpha} = 0.5°$, and a mean value of the pitch angle, $\alpha_m = 0\ 37°$. The range of reduced frequency k was taken from 0.05 to 0.2, and the Mach and Reynolds numbers were held fixed at $M_\infty = 0\ 75$ and $Re = 11.4 \times 10^6$, respectively (Table 1).

Computations and Code Performance

Both inviscid and viscous unsteady computations were carried out for the flow conditions previously outlined Viscous computations were based on both the thin-layer and the full Navier-Stokes equations The computational grids have a common outer boundary located 8 chord lengths above and below the airfoil leading edge with the airfoil at $\alpha = 0$. The domain of the grid in the upstream and downstream directions was set to 8 chord lengths from the airfoil leading edge.

A grid having 139×49 points in the ξ and η directions, respectively, was used throughout the computation on the Cray-XMP computer at Ames. The airfoil configurations were described with 117 grid points The computations were started from a steady-flow solution obtained at neutral position of airfoil oscillation, computations were continued through three cycles of oscillation to reach a periodic solution.

Including the viscous terms requires additional computational effort per grid point, and the fine mesh, needed to resolve the boundary-layer region, necessitated a smaller time-step than the one used in the inviscid computations. Decreasing the frequency of the airfoil oscillations also requires an increased number of iterations per cycle to maintain the time-accuracy requirement of the Courant number For airfoil oscillations at a reduced frequency, $k = 0.2$, the computation required 2620 iterations per cycle, whereas at $k = 0\ 05$ and 0 025, the computation required 4320 iterations per cycle. With vectorized codes on the Cray-XMP Computer, the required computational time per iteration for 139×49 grid points was 0.3 sec for the full Navier-Stokes code, 0.22 sec for the thin-layer Navier-Stokes code, and 0.17 sec for the inviscid computations.

Instantaneous Surface-Pressure and Shock-Wave Excursion

Case NACA 64A010 at low incidence, $\alpha = 0° + 1° \cos \omega t$, k = 0.025 and 0.20 (Table 1, Fig. 3).

Computed and experimental surface-pressure distributions, obtained as the airfoil angle of attack varied harmonically from 1° to -1° at k = 0 2, are shown in Fig. 3. Computations are shown for the thin-layer form of the Navier-Stokes equations. Results are presented for only one-half cycle of oscillation, since the motion is symmetrical. At the extreme angle of attack, $\alpha = 1°$, a supersonic region is evident on the upper surface that terminates in a shock at x/c = 0 55. As the angle of attack decreases, the flow speed gradually decreases on the upper surface, with corresponding increases in pressure At the same time, the shock strength decreases, as evidenced by the decrease of the pressure rise at the shock By contrast, the flow speed on the lower surface of the airfoil increases, resulting in reduced surface pressures and a reversed flow pattern The comparisons of the computational results (with free-stream boundary condition) and the experimental measurements show that the computed pressures ahead of the upper-surface shock are underpredicted. The studies reported in Refs 18 and 19 and the computation with the experimentally measured wall-pressure boundary-condition of Refs 8 and 20 indicate that this underprediction of the pressure is in part a result of the wind-tunnel-wall interference The pressure distributions downstream of the shock where the flow is not separated are well predicted

Computed and experimentally measured time-variations of the local pressure coefficient on the upper surface of the airfoil for a complete cycle of oscillation at k = 0 025 and 0 20 are shown in Fig. 4. In this case, results from all three forms of the equation (inviscid, thin-layer, and full Navier-Stokes) are all in good agreement The surface pressures display sinusoidal variations ahead of the shock wave (points A, B, and C), and nonlinear variation in the shock region (point D). The pressures also show hysteretic variations at the higher frequency, k = 0 2. Significant hysteresis is evident at point D in the shock region where the pressure undergoes a jump (indicating the passing-over of the shock wave) during decreasing angle of attack and smooth-pressure recovery during increasing angle of attack The computational results shown in Fig 4 using the inviscid and viscous approximations are all in good agreement with experimental data that indicate that viscous effects are small in these flow regimes

The loci of the computed and measured shock-wave excursions are depicted in Fig 5, which shows that the shock moves linearly with the airfoil motion and travels over approximately 7% of the chord with the midchord as neutral position (approximately) The trend of the excursions is well predicted by either the inviscid- or viscous-flow computations. The results of the viscous computation, however, agree better with the experimental data

Case NACA 64A010 at high incidence, $\alpha = 4° + 1° \cos \omega t$, k = 0 20 (Table 1, Fig 6).

This case is different from the previous case of low-incidence flow mainly in respect to the mean angle of attack, it is concerned with a flow strongly governed by shock-wave/boundary-layer interactions and a moving shock wave with greater strength variation (cf Refs. 16 and 21 for details). The test also showed that for k = 0 2, shock-induced separated flow is present for most angles of attack

Computed surface-pressure distributions based on both of the viscous (full and thin-layer) assumptions are shown in Fig 6 as the airfoil angle of attack is varied from 5° to 3° and back to 5° For inviscid computations, only typical instantaneous pressures at $\alpha = 5°$ are shown in Fig 6(a), for the pressure distributions retain about the same features during the angle-of-attack variation and are not in good agreement with the experimental data Also shown in Fig 6 are the experimentally measured pressure distributions. Within this angle-of-attack range, a supersonic region is evident only on the upper airfoil surface, whereas, on the lower surface the flow remains subsonic. Only a typical lower-surface-pressure distribution is shown in Fig 6(a), for it does not vary significantly with airfoil motion

An examination of the experimental data in Fig 6, starting with the airfoil leading edge on the upper surface, shows that the pressure decreases rapidly within a short distance from the leading edge (x/c = 0 ~ 0 05) to a fairly level plateau The computed results of this plateau pressure level by both the inviscid and viscous models are all in fairly good agreement with one another, in spite of the large discrepancy among the theories in the region downstream of the shock wave This indicates that downstream effects, including shock-wave discontinuities and shock-wave/boundary-layer interactions have little effect on the plateau pressure (or supersonic) region of the airfoil In a manner similar to that of the low-incidence case, the computed pressures ahead of the shock are underpredicted in part because of the wind-tunnel-wall interference Recent experiments show that the interference was more significant as the incidence of the flow to the airfoil is increased (Refs 18 and 19).

The comparisons of the inviscid computations and the experimental measurements show that the shock strength is overestimated and that the computed shock wave is positioned too far downstream when the inviscid theory is used The computed results with the full and the thin-layer Navier-Stokes equations showed no significant difference in the magnitude of instantaneous surface pressures Although the location of the shock wave differs by about 0%-3% of the chord, neither computation gave consistently closer agreement with experimentally measured surface pressures over the entire range of the airfoil oscillation.

Also shown in Fig 6 is the measured upper-surface-pressure distribution, it shows an aft-shock pressure recovery A slow pressure recovery is typified by a pressure distribution with a large bump behind the shock wave, such as those shown in Fig 6(a) for $\alpha = 5°$, a fast recovery is typified by a smooth pressure increase, such as those for $\alpha = 3\ 13°$ (Fig. 6(h)). The aft-shock pressure bump is indicative of probable flow separation induced by the shock-wave/boundary-layer interactions, whereas the fast pressure recovery indicates probable attached flow on the airfoil surface behind the shock wave. Steady flow interferograms obtained by Johnson and Bachalo (Ref 21) on the same airfoil under the same flow condition show extensive shock-induced separation for $\alpha = 5°$ and attached flow for $\alpha = 3°$ (unpublished data) in the aft shock region. The measured pressure variations aft of the shock wave in Fig 6 show that a slow pressure recovery (indicative of separated flow) is maintained for most of the angle-of-attack variation, except in the upward motion of the airfoil when the angle of attack is varied from 3° to 3 13° Fairly good agreement between the computed and the measured pressure recovery was obtained with the Navier-Stokes equations Although the transition angle of attack between the slow and fast pressure recoveries (indicative of separated and attached flow, respectively) is not

accurately predicted, some of the important effects of the shock-induced separation and the shock-wave/boundary-layer interactions are clearly demonstrated by the aft-shock pressure distribution in Fig 6. Typically, Fig. 6(b) depicts a slow aft-shock pressure recovery at α = 4 87°. The corresponding computed instantaneous velocity vectors depicted in Fig. 7 show shock-induced separation at the same angle of attack.

Figure 8 shows instantaneous pressure distributions on the airfoil upper surface when the angle of attack is increasing or decreasing and passing through the neutral position α = 4°. The results exhibit a substantial phase shift of the pressure relative to the airfoil motion, the shock positions differ by about 10% of the chord, and the flow aft of the shock is separated during decreasing angle-of-attack motion and is attached during increasing angle-of-attack motion.

The loci of the computed and measured shock-wave excursions are depicted in Fig. 9, which shows that the shock travels over approximately 13% of the chord length, with the neutral position at about x/c = 0.45. In this figure, some of the important features of unsteady transonic flow at high incidence are depicted. For a flow without separation, such as the case of low flow-incidence (Fig. 5), and in accordance with inviscid theories, the shock wave moves downstream with increasing angle of attack. In this case, however, the shock wave initially moves downstream with increasing angle of attack (from 3° to 5°), but starts to move upstream at 4.8° owing to the occurrence of flow separation, as was indicated in Fig. 6(1) and 6(a) by the appearance of slow aft-shock pressure recovery. It appears that this important "retrograde" shock motion cannot be predicted with inviscid transonic theories.

The results of the "thin-layer" computations shown in Ref. 6 differ somewhat from those shown in Fig. 6. In the present computation, grid spacing was densely clustered near the airfoil surface (about two grid points in the sublayer) to more accurately compute the eddy-viscosity terms in the turbulence model.

Case NLR 7301 at low incidence, α = 0 37° + 0.5° cos ωt, k = 0.05 and 0.20 (Table 1, Fig. 10).

Figure 10 shows data for a flow that differs from the previously considered flow in terms of airfoil geometry, pitch-axis location, and amplitude of oscillation. The NLR 7301 airfoil was designed for "shock-free" flow and is an example of a relatively thick (t/c = 0.165) modern supercritical airfoil (Refs. 22 and 23) Experimental data show that the flow was shock-free at M_∞ = 0.75 as the airfoil was held fixed at α = 0.37°. At off-design condition, as in this case, experimental data in Fig. 10 show that a weak shock was evident on the airfoil upper surface.

Both the computed and the experimentally measured pressures show small variations, relative to the cases of the NACA 64A010 airfoil previously studied, because of the oscillatory motion. Thus, only the instantaneous pressures at the extremes of angle of attack are shown in Fig. 10. The pressure variations in Fig. 10 show a pressure rise to a plateau level immediately after the leading edge owing to the blunt and thick leading section of the supercritical airfoil. Unlike the conventional airfoil, wavy pressure distributions are shown in Fig 10 in the plateau region (x/c = 0.1 ~ 0 6). The time-variation of the computed and measured local pressures in the plateau region also show small unsteady pressure fluctuations (or higher harmonic component) in addition to the overall pressure variation, indicating that the supercritical airfoil is very sensitive to the unsteady effects from the flow field. Although these small pressure variations in the plateau region are not computationally well predicted, the computational results in Fig. 10 show the general feature of the pressure typical to the supercritical airfoil. Comparison of pressures at the extremes of angle of attack between the two frequencies (k = 0.5 and 0 20) indicates that the pressures are less sensitive to the airfoil motion at higher frequency. At lower frequency, k = 0.05, only those pressures in the plateau region are affected by the airfoil motion.

Harmonic Analysis of Unsteady Pressures

Both computed and measured unsteady pressures have been expressed in Fourier components up to and including the third harmonic The higher harmonic components are not presented in the following figures since the modal content decreases rapidly with increasing mode number Distinctive features of the pressures depicted in Figs. 11-14 are discussed in the following paragraphs

Case. NACA 64A010 at low incidence, α = 0° + 1° cos ωt, k = 0.025 and 0.20 (Table 1, Fig. 11)

Illustrated here are the basic characteristics of the unsteady surface pressure for the conventional airfoil as it is subjected to a flow with small flow-incidence or a weak shock-wave/boundary-layer interaction or both. The mean-pressure features a distribution similar to those of steady flow, and is reasonably well predicted except in the shock region, where the viscous computations show closer agreement with the experimental data.

Examination of the higher frequency (k = 0.2), in-phase (Re) and out-of-phase (Im) components indicates that the pressures forward of the shock wave (x/c < 0 5) contain both components in about equal magnitude. Pressures behind the shock wave, however, contain mostly out-of-phase components. In the low-frequency case (k = 0.025), pressures in front of the shock wave contain more in-phase than out-of-phase contributions, whereas behind the shock wave both components are small and of about the same magnitude. The out-of-phase components for both frequencies, k = 0.025 and 0.2, also show that the component in front of the shock is 180° out-of-phase with those behind the shock, and a rapid phase shift abruptly takes place at the shock. At both frequencies, the real and imaginary components shown in Fig. 11 and the measured data for other frequencies (Ref. 9) exhibit similar distributions over the airfoil surface and indicate that the variation of the components is approximately linear with the frequency in the flow for which shock-wave/boundary-layer interactions are minimal.

Case. NACA 64A010 at high incidence, α = 4° + 1° cos ωt, k = 0.05 and 0.20 (Table 1, Fig. 12).

The high-incidence flow (α_m = 4°) considered here differs from the low-incidence case (α_m = 0°) in the mean angle of attack and is characterized by dominant shock-wave/boundary-layer interactions. The mean unsteady pressure shown in Fig. 12 exhibits a rapid decrease from the airfoil leading edge to a plateau pressure level ahead of the shock. It also shows an abrupt pressure jump at the shock region followed by a slow

pressure recovery (indicative of separated flow). Only the mean values of the pressure computed with inviscid assumption for $k = 0.2$ are depicted in Fig 12. It shows that the predicted shock position is too far downstream.

Examination of the harmonic components of the pressure for the high-frequency case, $k = 0.2$ in Fig. 12, indicates that the upper-surface pressure in front of the shock wave contains both in-phase (real part) and out-of-phase (imaginary part) components of about equal magnitude, however, the pressure immediately behind the shock wave ($x/c = 0.6$) contains mostly in-phase components Toward the airfoil trailing edge ($x/c = 0.6 - 0.9$), the pressure increases gradually in its in-phase and rapidly in its out-of-phase components In the trailing-edge region, the pressures contain mostly out-of-phase components. The variation to these harmonic components behind the shock distinguishes the present case from the previous case (low-incidence flow) where the flow behind the shock wave is attached and the pressure contains only the out-of-phase components

The effects of frequency can be evaluated by comparing the harmonic components of the pressure for both $k = 0\ 05$ and $0\ 2$ in Fig. 12. This comparison indicates that the surface pressure at the lower frequency $k = 0\ 05$ contains mostly in-phase components. In the shock region, the in-phase components at the lower frequency are 180° out of phase with those at the higher frequency Toward the airfoil trailing edge, the in-phase components rapidly decrease at the lower frequency, whereas they exhibit the opposite trend (gradually decrease) at the higher frequency. These nonlinear variations of the harmonic components with frequency differ distinctly from those previously considered in low-incidence flow, particularly in the shock wave and in the aft-shock separated regions of airfoil surface They also show strong nonlinear variations with frequency, thus reflecting the complex effects from shock-wave/boundary-layer interactions and shock-induced separation

Pressure variations on the lower airfoil surface in Fig. 12 do not exhibit variations as rapid as those on the upper surface. The harmonic components of the pressure show a nearly linear variation from the leading to the trailing edges of the airfoil

Case NLR 7301 at low incidence, $\alpha = 0\ 37° + 0.5° \cos \omega t$, $k = 0\ 05$ and 0.20 (Table 1, Figs. 13-14).

The case considered here differs from the previous studies in the airfoil geometry Figure 13 shows a plateau in the mean pressure that is reached rapidly from the blunt leading edge of the thick airfoil and that is sustained up to the region of rapid compression (but not a shock) on the airfoil ($x/c = 0\ 6$). The mean unsteady pressure in the aft-region of compression exhibits a rapid pressure recovery that indicates an unseparated flow

The harmonic components of pressure show that the pressure in the fore section of the airfoil contains both in-phase and out-of-phase components of about the same magnitude (as in the NACA 64A010 in high incidence flow, and at $k = 0\ 2$ only, Fig 12) The magnitude of these components is significantly increased at about 60% of the chord, a result of the occurrence of rapid compression.

Comparison of the harmonic components of the pressure for both frequencies, $k = 0\ 2$ and $0\ 05$, indicates that the out-of-phase components do not diminish at a lower frequency, but remain at about the same magnitude in both frequencies This is contrary to the case of the conventional airfoil (Figs 11 and 12). The in-phase components, however, show an increase in magnitude at a lower frequency that is comparable to that seen in the case of the conventional airfoil.

The computed magnitudes of the harmonic components (Fig 13) exhibit only the qualitative trends of the experimentally determined pressure variations However, it should be noted that the computation assumed uniform free-stream boundary conditions and the wind-tunnel-wall effects were not taken into account Measured pressure signatures, on the other hand, can be affected by the wind-tunnel-wall interference (Ref 8) and by a small change in free-stream turbulence level in different wind tunnels (Refs 16 and 22) Experiments show that the pressure is also sensitive to geometry even at such small protuberances as a pressure transducer in the shock region The mathematically smoothed, measured airfoil profile used in the present computation could lead to the discrepancies.

The phases of the complex pressure components for both frequencies, $k = 0\ 2$ and $0\ 05$, are shown in Fig. 14, good agreement with experimental data is shown The figure also shows that phase varied gradually in the leading section of the airfoil and jumped abruptly at $x/c = 0\ 6$.

Surface pressures on the airfoil lower surface were not experimentally measured However, the computational results shown in Fig. 13 show that the harmonic components are minimal on the rear half (concaved portion) of the airfoil lower surface for the flow conditions investigated.

The overall pressure distributions displayed in Figs. 13-14 show that the unsteady air loads on the supercritical airfoil are distinctly different from those on the conventional airfoil

CONCLUSION

The ability of a Navier-Stokes code to compute unsteady transonic flow over an airfoil in oscillatory motion has been investigated in conjunction with a series of tests conducted in the 11- by 11-Foot Transonic Wind Tunnel at Ames Research Center. Two airfoils were considered, a conventional (NACA 64A010) and a supercritical (NLR 7301) section. The study of the conventional airfoil disclosed that the unsteady flow field and the related aerodynamic load, both in cases of low and moderately high flow incidence, were fairly well predicted The computed results successfully and distinctly demonstrated the nonlinear aerodynamics characterized by the shock-wave/boundary-layer interactions and frequency of the airfoil motion The inviscid Euler code was shown to be adequate only in the case of low-incidence flow, or for the flow in which viscous effects are minimal For the supercritical airfoil, only the computed mean unsteady pressures and phase of the Fourier components are in good agreement with the experimental data The harmonic magnitudes of the pressure, which are experimentally, as well as theoretically, shown to be extremely sensitive in the transonic regime for supercritical airfoils, are predicted in a qualitative manner only The difficulties in correlating computed results with experimental data in this case could be attributed to the sensitive characteristics of the

supercritical airfoil. In summary, the Navier-Stokes code demonstrated fairly well its capability of modeling the nonlinear, unsteady aerodynamics for a supercritical airfoil.

The Navier-Stokes computations with and without the thin-layer approximation showed no noticeable difference in the magnitude of instantaneous airfoil surface pressures, except in the location of the shock wave, which differs by 0%-3% of the chord. Neither computation gave consistently better or closer agreement with experimentally measured surface pressure. A substantial difference in shock position was shown in Ref. 6, where insufficient clustering of the grid was made in the sublayer of the turbulent boundary layer in the thin-layer Navier-Stokes computations.

The present code uses an eddy-viscosity model for the turbulent boundary layer that was developed using simple steady-flow experiments. For unsteady, high-incidence flow for which viscous effects dominate, an improved turbulence model is surely required. However, the demonstrated capability of the code has important implications for applications in aeroelastic and control-response analyses and in the study of wake-airfoil interactions.

REFERENCES

1 Beam, R , and Warming, R. F An Implicit Finite Difference Algorithm for Hyperbolic Systems in Conservation Law Form. J. Comput. Phys., vol. 22, Sept. 1976, pp. 87-110.

2 Steger, J L Implicit Finite-Difference Simulation of Flow about Arbitrary Two-Dimensional Geometries AIAA J , vol 16, no. 7, July 1978, pp. 679-686

3. Steger, J. L , and Bailey, H. E Computations of Transonic Flow over an Airfoil with Shock-Induced Separation AIAA J., vol. 18, Mar. 1980, pp 249-255.

4. Chyu, W. J., Davis, S. S., and Chang, K. S Calculation of Unsteady Transonic Flow over an Airfoil. AIAA J., vol. 19, no. 6, June 1981, pp. 684-690.

5 Chyu, W. J., and Schiff, L B. Nonlinear Aerodynamic Modeling of Flap Oscillations in Transonic Flow A Numerical Validation. AIAA J., vol. 21, No. 1, Jan. 1983, pp. 106-113

6. Chyu, W J., and Kuwahara, K. Computations of Transonic Flow over an Airfoil with Shock-Induced Separation. AIAA Paper 82-0350, 1982.

7 Chyu, W. J., and Ono, K. Unsteady Transonic Flow over Conventional and Supercritical Airfoils AIAA Paper 83-0235, 1983

8. Horiuti, K , Chyu, W J., and Buell, D A. Unsteady, Transonic Flow Computations for an Airfoil with an Oscillating Flap. AIAA Paper 84-1562, 1984.

9 Davis, S. S. Data Set 2, NACA 64A010 (NASA Ames Model) Oscillatory Pitching Data Set 5, NLR 7301 Supercritical Airfoil Oscillatory Pitching. AGARD Report No 702, Compendium of Unsteady Aerodynamic Measurements, edited by AGARD/SMP Subcommittee on Aeroelasticity, Aug. 1982.

10. Baldwin, B. S , and Lomax, H.. Thin Layer Approximation and Algebraic Model for Separated Turbulent Flows AIAA Paper 78-257, 1978.

11 Sorenson, R. L , and Steger, J. L. Simplified Clustering of Nonorthogonal Grids Generated by Elliptic Partial Differential Equations NASA TM-73252, 1977.

12. Malcolm, G., and Davis, S. S New NASA Ames Wind Tunnel Techniques for Studying Airplane Spin and Two-Dimensional Unsteady Aerodynamics in Dynamic Stability Parameters AGARD CP-235, Nov. 1978, pp 3-1 to 3-12

13. Davis S. S Computer/Experiment Integration for Unsteady Aerodynamic Research. Congress on Instrumentation in Aerospace Simulation Facilities, ICIASF, 1979 Record, Sept 1979, pp. 237-250.

14. Davis, S. S., and Malcolm, G. Unsteady Aerodynamics of Conventional and Supercritical Airfoils. AIAA Paper 80-734, 1980.

15. Davis, S. S., and Malcolm, G. Experimental Unsteady Aerodynamics of Conventional and Supercritical Airfoils. NASA TM-81221, 1980.

16 Davis, S S , and Malcolm, G. Transonic Shock-Wave/Boundary-Layer Interactions on an Oscillating Airfoil. AIAA J , vol. 18, no 11, Nov 1980, pp. 1306-1312.

17. Davis, S. S. Experimental Studies of Scale Effects on Oscillating Airfoils at Transonic Speeds AGARD-CP-296, Feb 1981, pp. 9-1 to 9-6

18 Buell, D A., and Malcolm, G. N An Experimental Investigation of the Aerodynamics of an NACA 64A010 Airfoil-Flap Combination with and without Flap Oscillations. Pt. 1 Steady State Characteristics. Proposed NASA TM.

19. Buell, D. A., and Malcolm, G. N. An Experimental Investigation of the Aerodynamics of an NACA 64A010 Airfoil-Flap Combination with and without Flap Oscillations Pt. II. Dynamic Characteristics. Proposed NASA TM

20 King, L. S., and Johnson, D. A. Calculations of Transonic Flow about an Airfoil in a Wind Tunnel. AIAA Paper 80-1366, 1980.

21. Johnson, D. A , and Bachalo, W. D . Transonic Flow about a Two-Dimensional Airfoil—Inviscid and Turbulent Flow Properties. AIAA J., vol. 18, no 1, Jan 1980, pp. 16-24.

22 Rohne, B. Data Report of a Wind Tunnel Investigation on Airfoil Section NLR 7301. NLR TR-74079 U, 1976, NLR, Amsterdam, Netherlands.

23. Zwaaneld, J. Aerodynamic Characteristics of the Supercritical Shock-Free Airfoil Section NLR 7301. NLR TR 76052 C, 1976, NLR, Amsterdam, Netherlands.

APPENDIX

The Navier-Stokes equations in Cartesian coordinates can be written as (Ref. 2)

$$\partial_t \bar{q} + \partial_x \bar{E} + a_y \bar{F} = Re^{-1}(\partial_x \bar{R} + \partial_y \bar{S}) \tag{A1}$$

where

$$\bar{q} = \begin{pmatrix} \rho \\ \rho u \\ \rho v \\ e \end{pmatrix}, \quad \bar{E} = \begin{pmatrix} \rho u \\ \rho u^2 + p \\ \rho uv \\ u(e + p) \end{pmatrix}, \quad \bar{F} = \begin{pmatrix} \rho v \\ \rho uv \\ \rho v^2 + p \\ v(e + p) \end{pmatrix}, \quad \bar{R} = \begin{pmatrix} 0 \\ \tau_{xx} \\ \tau_{xy} \\ R_4 \end{pmatrix}, \quad \bar{S} = \begin{pmatrix} 0 \\ \tau_{xy} \\ \tau_{yy} \\ S_4 \end{pmatrix}$$

where

$$\begin{aligned}
\tau_{xx} &= (\lambda + 2\mu)u_x + \lambda v_y \\
\tau_{xy} &= \mu(u_y + v_x) \\
\tau_{yy} &= (\lambda + 2\mu)v_y + \lambda u_x \\
R_4 &= u\tau_{xx} + v\tau_{xy} + \kappa Pr^{-1}(\gamma - 1)^{-1}\partial_x a^2 \\
S_4 &= u\tau_{xy} + v\tau_{yy} + \kappa Pr^{-1}(\gamma - 1)^{-1}\partial_y a^2 \\
p &= (\gamma - 1)\left[e - \frac{1}{2}\rho(u^2 + v^2)\right] \\
a^2 &= \gamma(\gamma - 1)\left[\frac{e}{\rho} - \frac{1}{2}(u^2 + v^2)\right]
\end{aligned}$$

and the Stokes hypothesis $\lambda + (2/3)\mu = 0$ is assumed. Equation (A1), subject to the general transformation, $\xi = \xi(x,y,t)$, $\eta = \eta(x,y,t)$, and $\tau = t$, gives

$$\partial_\tau \hat{q} + \partial_\xi(\hat{E} - \hat{R}) + \partial_\eta(\hat{F} - \hat{S}) = 0 \tag{A2}$$

where

$$\begin{aligned}
\hat{q} &= \bar{q}/J \\
\hat{E} &= (\xi_t \bar{q} + \xi_x \bar{E} + \xi_y \bar{F})/J \\
\hat{F} &= (\eta_t \bar{q} + \eta_x \bar{E} + \eta_y \bar{F})/J
\end{aligned}$$

and chain rule is applied to stress terms such as $\tau_{xx} = (\lambda + 2\mu)(\xi_x u_\xi + \eta_x u_\eta) + \lambda(\xi_y v_\xi + \eta_y v_\eta)$, etc. The viscous dissipation vectors in Eq (A2) are

$$\begin{aligned}
\hat{R} &= J^{-1}Re^{-1}(\xi_x \bar{R} + \xi_y \bar{S}) \\
\hat{S} &= J^{-1}Re^{-1}(\eta_x \bar{R} + \eta_y \bar{S})
\end{aligned}$$

where

$$\bar{R} = [0, \tau_{xx}, \tau_{xy}, R_4]^T, \quad \bar{S} = [0, \tau_{xy}, \tau_{yy}, S_4]^T$$

The viscous vectors, $\hat{R}$ and $\hat{S}$, contain terms that are functions of $(\hat{q}, \hat{q}_\xi)$ and $(\hat{q}, \hat{q}_\xi)$, and are written as

$$\begin{aligned}
\hat{R}(\hat{q}, \hat{q}_\xi, \hat{q}_\eta) &= \hat{R}_1(\hat{q}, \hat{q}_\xi) + \hat{R}_2(\hat{q}, \hat{q}_\eta) \\
\hat{S}(\hat{q}, \hat{q}_\xi, \hat{q}_\eta) &= \hat{S}_1(\hat{q}, \hat{q}_\xi) + \hat{S}_2(\hat{q}, \hat{q}_\eta)
\end{aligned}$$

where

$$\hat{R}_1(\hat{q}, \hat{q}_\xi) = Re^{-1}J^{-1}\begin{bmatrix} 0 \\ \alpha_1 u_\xi + \alpha_3 v_\xi \\ \alpha_3 u_\xi + \alpha_2 v_\xi \\ \frac{\alpha_1}{2}(u^2)_\xi + \frac{\alpha_2}{2}(v^2)_\xi + \alpha_3(uv)_\xi + \alpha_4(\gamma - 1)^{-1}(a^2)_\xi \end{bmatrix}$$

$$\hat{R}_2(\hat{q},\hat{q}_\eta) = Re^{-1}J^{-1}\begin{bmatrix} 0 \\ \gamma_1 u_\eta + \gamma_3 v_\eta \\ \gamma_4 u_\eta + \gamma_2 v_\eta \\ \frac{\gamma_1}{2}(u^2)_\eta + \frac{\gamma_2}{2}(v^2)_\eta + \gamma_3 u v_\eta + \gamma_4 v u_\eta + \gamma_5(\gamma - 1)^{-1}(a^2)_\eta \end{bmatrix}$$

$$\hat{S}_1(\hat{q},\hat{q}_\xi) = Re^{-1}J^{-1}\begin{bmatrix} 0 \\ \gamma_1 u_\xi + \gamma_4 v_\xi \\ \gamma_3 u_\xi + \gamma_2 v_\xi \\ \frac{\gamma_1}{2}(u^2)_\xi + \frac{\gamma_2}{2}(v^2)_\xi + \gamma_4 u v_\xi + \gamma_3 v u_\xi + \gamma_5(\gamma - 1)^{-1}(a^2)_\xi \end{bmatrix}$$

$$\hat{S}_2(\hat{q},\hat{q}_\eta) = Re^{-1}J^{-1}\begin{bmatrix} 0 \\ \beta_1 u_\eta + \beta_3 v_\eta \\ \beta_3 u_\eta + \beta_2 v_\eta \\ \frac{\beta_1}{2}(u^2)_\eta + \frac{\beta_2}{2}(v^2)_\eta + \beta_3(uv)_\eta + \beta_4(\gamma - 1)^{-1}(a^2)_\eta \end{bmatrix}$$

Here,

$$\alpha_1 = \mu(\xi_y^2 + \tfrac{4}{3}\xi_x^2) \qquad \beta_1 = \mu(\eta_y^2 + \tfrac{4}{3}\eta_x^2) \qquad \gamma_1 = \mu(\xi_y\eta_y + \tfrac{4}{3}\xi_x\eta_x)$$

$$\alpha_2 = \mu(\xi_x^2 + \tfrac{4}{3}\xi_y^2) \qquad \beta_2 = \mu(\eta_x^2 + \tfrac{4}{3}\eta_y^2) \qquad \gamma_2 = \mu(\xi_x\eta_x + \tfrac{4}{3}\xi_y\eta_y)$$

$$\alpha_3 = \tfrac{\mu}{3}\xi_x\xi_y \qquad \beta_3 = \tfrac{\mu}{3}\eta_x\eta_y \qquad \gamma_3 = \mu(\xi_y\eta_x - \tfrac{2}{3}\xi_x\eta_y)$$

$$\alpha_4 = \kappa Pr^{-1}(\xi_x^2 + \xi_y^2) \qquad \beta_4 = \kappa Pr^{-1}(\eta_x^2 + \eta_y^2) \qquad \gamma_4 = \mu(\xi_x\eta_y - \tfrac{2}{3}\xi_y\eta_x)$$

$$\gamma_5 = \kappa Pr^{-1}(\xi_x\eta_x + \xi_y\eta_y)$$

In terms of the viscous terms $\hat{R}_1$, $\hat{R}_2$, $\hat{S}_1$, $\hat{S}_2$, Eq (A2) is reduced to

$$\partial_\tau\hat{q} + \partial_\xi\hat{E} + \partial_\eta\hat{F} = \partial_\xi(\hat{R}_1 + \hat{R}_2) + \partial_\eta(\hat{S}_1 + \hat{S}_2) \tag{A3}$$

A solution to Eq (A3) can be obtained by using a single-step temporal scheme (Ref. 1)

$$\Delta\hat{q}^n = \frac{\theta\,\Delta\tau}{1+\beta}\,\partial_\tau\,\Delta\hat{q}^n + \frac{\Delta\tau}{1+\beta}\,\partial_\tau\hat{q}^n + \frac{\beta}{1+\beta}\,\Delta\hat{q}^n + O\left[\left(\theta - \frac{1}{2} - \beta\right)\Delta\tau^2 + \Delta\tau^3\right] \tag{A4}$$

where $\Delta\hat{q}^n = \hat{q}^{n+1} - \hat{q}^n$, $\hat{q}^n = \hat{q}(n\,\Delta\tau)$, and n denotes the nth time step of computations The implicit trapezoidal scheme takes $\theta = 1/2$ and $\beta = 0$ in (A4) which results in truncation error $O(\Delta\tau^3)$, and the implicit Euler scheme takes $\theta = 1$ and $\beta = 0$ which is $O(\Delta\tau^2)$. The implicit trapezoidal scheme was used in the present computations.

Applying the scheme (A4) into Eq (A3), one obtains a solution to the Navier-Stokes equations

$$\Delta\hat{q}^n = \frac{\theta\,\Delta\tau}{1+\beta}\,[\partial_\xi(-\Delta\hat{E}^n + \Delta\hat{R}_1^n + \Delta\hat{R}_2^n) + \partial_\eta(-\Delta\hat{F}^n + \Delta\hat{S}_1^n + \Delta\hat{S}_2^n)] + \frac{\Delta\tau}{1+\beta}\,[\partial_\xi(-\hat{E} + \hat{R}_1 + \hat{R}_2)^n$$

$$+ \partial\eta(-\hat{F} + \hat{S}_1 + \hat{S}_2)^n] + \frac{\beta}{1+\beta}\,\Delta\hat{q}^{n-1} + O[(\theta - \tfrac{1}{2} - \beta)\Delta\tau^2 + \Delta\tau^3] \tag{A5}$$

where $\Delta\hat{E}^n = \hat{E}^{n+1} - \hat{E}^n$ and $\hat{E}^{n+1} = \hat{E}(\hat{q}^{n+1})$, etc The finite-difference form of $\hat{q}^n$ is $\hat{q}^n_{i,j}$ at $x = i\,\Delta x$ and $y = i\,\Delta y$

The flux vector increments ($\Delta\hat{E}^n$, $\Delta\hat{F}^n$, $\Delta\hat{R}_1$, $\Delta\hat{R}_2$, $\Delta\hat{S}_1$, $\Delta\hat{S}_2$) are nonlinear functions of $\hat{q}$, and are linearized by using Taylor series expansion.

$$\begin{aligned} \Delta\hat{E}^n &= \hat{A}^n\,\Delta\hat{q}^n + O(\Delta\tau^2) \\ \Delta\hat{F}^n &= \hat{B}^n\,\Delta\hat{q}^n + O(\Delta\tau^2) \end{aligned} \tag{A6}$$

where $\hat{A}^n = (\partial\hat{E}/\partial\hat{q})^n$, $\hat{B}^n = (\partial\hat{F}/\partial\hat{q})^n$, or in detail

$$\hat{A} \text{ or } \hat{B} = \left[\begin{array}{c|c|c|c} k_0 & k_1 & k_2 & 0 \\ \hline -u(k_1u + k_2v) + k_1\phi^2 & -(\gamma - 3)k_1u + k_0 + k_2v & -(\gamma - 1)k_1v + k_2u & (\gamma - 1)k_1 \\ \hline -v(k_1u + k_2v) + k_2\phi^2 & -(\gamma - 1)k_2u + k_1v & -(\gamma - 3)k_2v + k_0 + k_1u & (\gamma - 1)k_2 \\ \hline (k_1u + k_2v)\left(-\frac{\gamma e}{\rho} + 2\phi^2\right) & \left(\frac{\gamma e}{\rho} - \phi^2\right)k_1 - (\gamma - 1)(k_1u + k_2v)u & \left(\frac{\gamma e}{\rho} - \phi^2\right)k^2 - (\gamma - 1)(k_1u + k_2v)v & \gamma(k_1u + k_2v) + k_0 \end{array}\right]$$

where $\phi^2 = (1/2)(\gamma - 1)(u^2 + v^2)$, and

$$k_0 = \xi_t\ , \quad k_1 = \xi_x\ , \quad k_2 = \xi_y \quad \text{for} \quad \hat{A}$$

$$k_0 = \eta_t\ , \quad k_1 = \eta_x\ , \quad k_2 = \eta_y \quad \text{for} \quad \hat{B}$$

Likewise, the linealization for $\Delta\hat{R}_1$ and $\Delta\hat{S}_2$ gives

$$\Delta\hat{R}_1^n = \hat{P}^n\ \Delta\hat{q}^n + \hat{K}^n\ \Delta\hat{q}_\xi^n + O(\Delta\tau^2)$$

$$\Delta\hat{S}_2^n = \hat{Q}^n\ \Delta\hat{q}^n + \hat{L}^n\ \Delta\hat{q}_\eta^n + O(\Delta\tau^2)$$

where $\hat{P}^n = (\partial\hat{R}_1/\partial\hat{q})^n$, $\hat{K}^n = (\partial\hat{R}_1/\partial\hat{q}_\xi)^n$, $\hat{Q}^n = (\partial\hat{S}_2/\partial\hat{q})^n$, and $\hat{L}^n = (\partial\hat{S}_2/\partial\hat{q}_\eta)^n$ The linearized $\Delta\hat{R}_1^n$ and $\Delta\hat{S}_2^n$ in the above can be further reduced to

$$\begin{aligned} \Delta\hat{R}_1^n &= (\hat{P} - \hat{K}_\xi)^n\ \Delta\hat{q}^n + \partial_\xi(\hat{K}\ \Delta\hat{q})^n + O(\Delta\tau^2) \\ \Delta\hat{S}_2^n &= (\hat{Q} - \hat{L}_\eta)^n\ \Delta\hat{q}^n + \partial_\eta(\hat{L}\ \Delta\hat{q})^n + O(\Delta\tau^2) \end{aligned} \tag{A7}$$

where $\hat{K}_\xi = \partial_\xi\hat{K}$ and $\hat{L}_\eta = \partial_\eta\hat{L}^n$. The viscous matrices $\hat{K}$, $\hat{L}$, $\hat{P} - \hat{K}_\xi$, and $\hat{Q} - \hat{L}_\eta$ are presented below.

$$\hat{K},\ \hat{L},\ (\hat{P} - \hat{K}_\xi),\ \text{or}\ (\hat{Q} - \hat{L}_\eta) = Re^{-1}\rho^{-1}\left[\begin{array}{c|c|c|c} 0 & 0 & 0 & 0 \\ \hline -h_1u - h_3v & h_1 & h_3 & 0 \\ \hline -h_3u - h_2v & h_3 & h_2 & 0 \\ \hline h_4\left(-\frac{e}{\rho} + u^2 + v^2\right) - h_1u^2 - 2h_3uv - h_2v^2 & (h_1 - h_4)u + h_3v & (h_2 - h_4)v + h_3u & h_4 \end{array}\right]$$

where

$$h_1 = \alpha_1\ , \quad h_2 = \alpha_2\ , \quad h_3 = \alpha_3\ , \quad h_4 = \alpha_4 \quad \text{for} \quad \hat{K}\ ,$$

$$h_1 = \beta_1\ , \quad h_2 = \beta_2\ , \quad h_3 = \beta_3\ , \quad h_4 = \beta_4 \quad \text{for} \quad \hat{L}\ ,$$

$$h_1 = \frac{\partial\alpha_1}{\partial\xi}\ , \quad h_2 = \frac{\partial\alpha_2}{\partial\xi}\ , \quad h_3 = \frac{\partial\alpha_3}{\partial\xi}\ , \quad h_4 = \frac{\partial\alpha_4}{\partial\xi} \quad \text{for} \quad \hat{P} - \hat{K}_\xi\ ,$$

and

$$h_1 = \frac{\partial\beta_1}{\partial\eta}\ , \quad h_2 = \frac{\partial\beta_2}{\partial\eta}\ , \quad h_3 = \frac{\partial\beta_3}{\partial\eta}\ , \quad h_4 = \frac{\partial\beta_4}{\partial\eta} \quad \text{for} \quad \hat{Q} - \hat{L}_\eta\ ,$$

The spatial derivatives $\partial\hat{R}_2/\partial\xi$ and $\partial\hat{S}_1/\partial\eta$ involve cross derivatives $\partial^2(\ )/\partial\xi\partial\eta$, in order to use a spatially factorized scheme, these terms are time-lagged as

$$\begin{aligned} \Delta\hat{R}_2^n &= \Delta\hat{R}_2^{n-1} + O(\Delta\tau^2) \\ \Delta\hat{S}_1^n &= \Delta\hat{S}_1^{n-1} + O(\Delta\tau^2) \end{aligned} \tag{A8}$$

Substitution from the linearized flux vector increments $\Delta\hat{E}^n$, $\Delta\hat{F}^n$, $\Delta\hat{R}_1^n$, $\Delta\hat{S}_2^n$ (A6 and A7) and the time lagged flux vector increments $\Delta\hat{R}_2^n$ and $\Delta\hat{S}_1^n$ (A8) to Eq. (A5) gives

$$\begin{aligned} &\left\{I + \frac{\theta\ \Delta\tau}{1 + \beta}\left[\partial_\xi(\hat{A} - \hat{P} + \hat{K}_\xi)^n - \partial_\xi^2\hat{K}^n + \partial_\eta(\hat{B} - \hat{Q} + \hat{L}_\eta)^n - \partial_\eta^2 L_\eta\right]\right\}\Delta\hat{q}^n \\ &\quad = \frac{\Delta\tau}{1 + \beta}\left[\partial_\xi(-\hat{E} + \hat{R}_1 + \hat{R}_2)^n + \partial_\eta(-\hat{F} + \hat{S}_1 + \hat{S}_2)^n\right] + \frac{\bar{\theta}\ \Delta\tau}{1 + \beta}\left[\partial_\xi(\Delta\hat{R}_2)^{n-1} + \partial_\eta(\Delta\hat{S}_1)^{n-1}\right] \\ &\quad + \frac{\beta}{1 + \beta}\ \Delta\hat{q}^{n-1} + O\left[\left(\theta - \frac{1}{2} - \beta\right)\Delta\tau^2, (\bar{\theta} - \theta)\Delta\tau^2, \Delta\tau^3\right] \end{aligned} \tag{A9}$$

Here, the notation of the form $[\partial_\xi(\hat{A} - \hat{P} + \hat{K}_\xi)]^n \Delta\hat{q}^n$ implies $\partial_\xi[(\hat{A} - \hat{P} + \hat{K}_\xi)^n \Delta\hat{q}^n]$, etc For second order accurate scheme $\bar{\theta}$ should be set to θ, and for first order accurate scheme $\bar{\theta}$ be set to zero.

The thin-layer approximation neglects terms $\partial_\xi^2\hat{K}^n$, $\partial_\xi(\hat{R}_1 + \hat{R}_2)$, $\partial_\eta\hat{S}_1$, $-\hat{P} + \hat{K}_\xi$, $-\hat{Q} + \hat{L}_\eta$, and $\partial_\xi(\Delta\hat{R}_2)^{n-1} + \partial_\eta(\Delta\hat{S}_1)^{n-1}$ in Eq. (A9).

Implementation of a spatially factored scheme in the left hand side of Eq. (A9) gives

$$\left\{I + \frac{\theta\,\Delta\tau}{1+\beta}\,[\partial_\xi(\hat{A} - \hat{P} + \hat{K}_\xi)^n - \partial_\xi^2\hat{K}^n]\right\}\left\{I + \frac{\theta\,\Delta\tau}{1+\beta}\,[\partial_\eta(\hat{B} - \hat{Q} + \hat{L}_\eta)^n - \partial_\eta^2\hat{L}^n]\right\}\Delta\hat{q}^n \equiv \mathrm{LHS(A9)} + O(\Delta\tau^3)$$

where LHS (A9) denotes the left hand side of Eq. (A9).

The following computational sequence is used to obtain the Navier-Stokes solutions

$$\left\{I + \frac{\theta\,\Delta\tau}{1+\beta}\,[\partial_\xi(\hat{A} - \hat{P} + \hat{K}_\xi)^n - \partial_\xi^2\hat{K}^n]\right\}\overline{\Delta\hat{q}^n} = \mathrm{RHS(A9)}$$

$$\left\{I + \frac{\theta\,\Delta\tau}{1+\beta}\,[\partial_\eta(\hat{B} - \hat{Q} + \hat{L}_\eta)^n - \partial_\eta^2\hat{L}^n]\right\}\Delta\hat{q}^n = \overline{\Delta\hat{q}^n} \qquad \text{(A10)}$$

$$\hat{q}^{n+1} = \hat{q}^n + \Delta\hat{q}^n$$

Equation (A10) can be simplified by assuming that the transport coefficients are locally constant, or $-\hat{P} + \hat{K}_\xi = -\hat{Q} + \hat{L}_\eta = 0$

The simplified form of Eq. (A10) is thus

$$\left\{I + \frac{\theta\,\Delta\tau}{1+\beta}\,[\partial_\xi(\hat{A} - \partial_\xi\hat{K})^n]\right\}\overline{\Delta\hat{q}^n} = \mathrm{RHS(A9)}$$

$$\left\{I + \frac{\theta\,\Delta\tau}{1+\beta}\,[\partial_\eta(\hat{B} - \partial_\eta\hat{L})^n]\right\}\Delta\hat{q}^n = \overline{\Delta\hat{q}^n}$$

$$\hat{q}^{n+1} = \hat{q}^n + \Delta\hat{q}^n$$

In the present computation, the time-lagged viscous term $\partial_\xi(\Delta\hat{R}_2)^{n-1} + \partial_\eta(\Delta\hat{S}_1)^{n-1}$ was neglected, reducing the order of the time-accuracy in the computation of dissipation terms from second to first order The final numerical algorithm constructed for the computations is thus first-order time-accurate for the dissipation and second-order time-accurate for the convection terms in the Navier-Stokes equations. The spatial derivatives in the equations were kept second-order accurate. This brief derivation differs from those of previous investigations by including all the relevant terms of the Navier-Stokes equations (Eq (A1))

TABLE 1. EXPERIMENTAL DATA THAT WILL BE COMPARED WITH COMPUTATIONAL RESULTS

Airfoil	Flow incidence	M_∞	Re × 10^{-6}	α_m, deg	$\tilde{\alpha}$, deg	k, $\omega c/2U_\infty$	Pitching axis, x/c
NACA 64A010	Low	0.8 0.8	12.0 12.0	0 0	1.0 1.0	0.025 0.20	0.25 0 25
	High	0.8 0.8	12.0 12.0	4 4	1.0 1.0	0.05 0.20	0.25 0.25
NLR 7301	Low	0.75 0.75	11.4 11.4	0 37 0 37	0.5 0.5	0.05 0.20	0.4 0.4

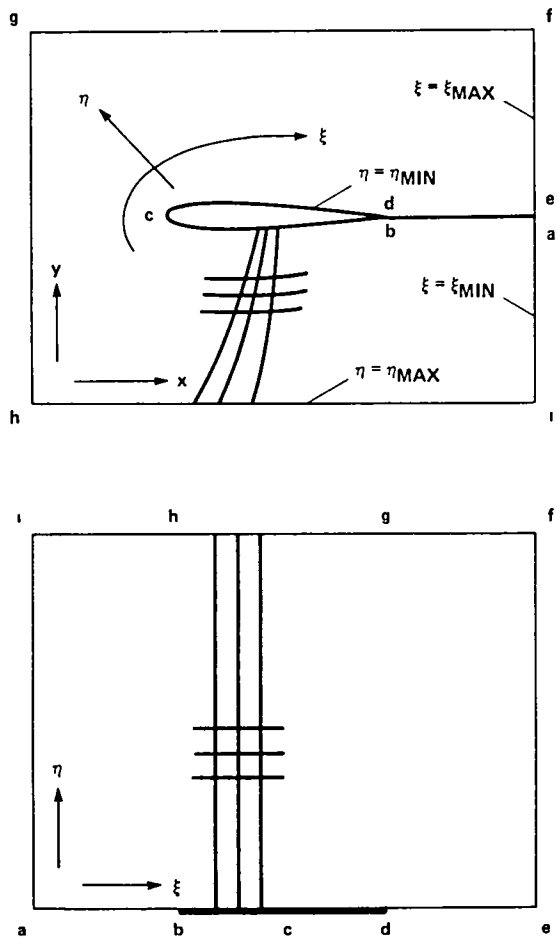

Fig. 1. Physical and computational planes.

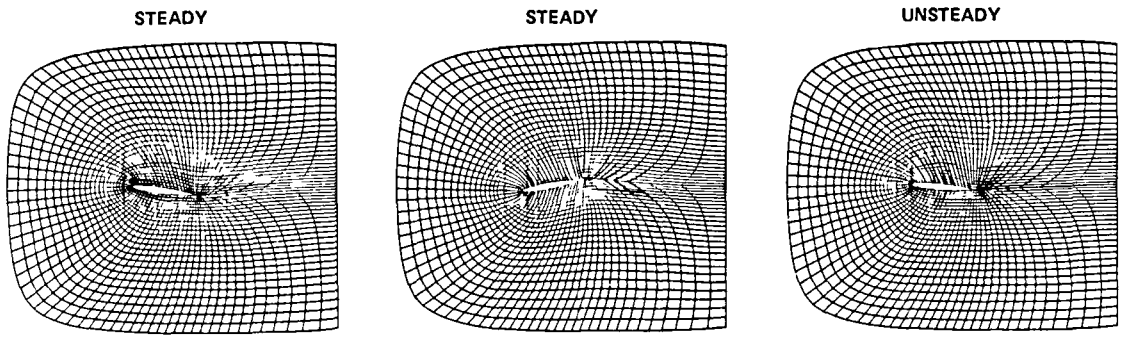

(a) Steady grids with airfoil at one extreme position.

(b) Steady grids with airfoil at another extreme position.

(c) Unsteady grids interpolated from (a) and (b).

Fig. 2 Unsteady grid interpolated from two steady-grid systems

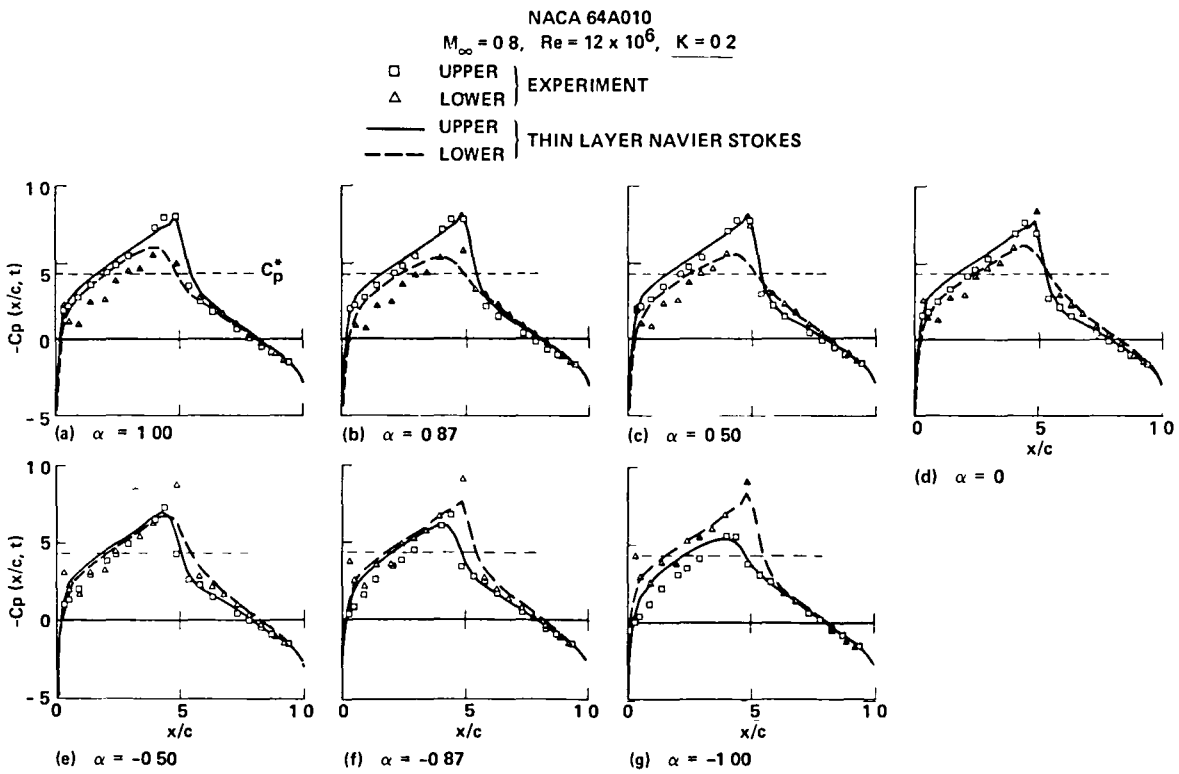

Fig 3. Surface-pressure variation with angle of attack, $\alpha = 0° + 1° \cos \omega t$.

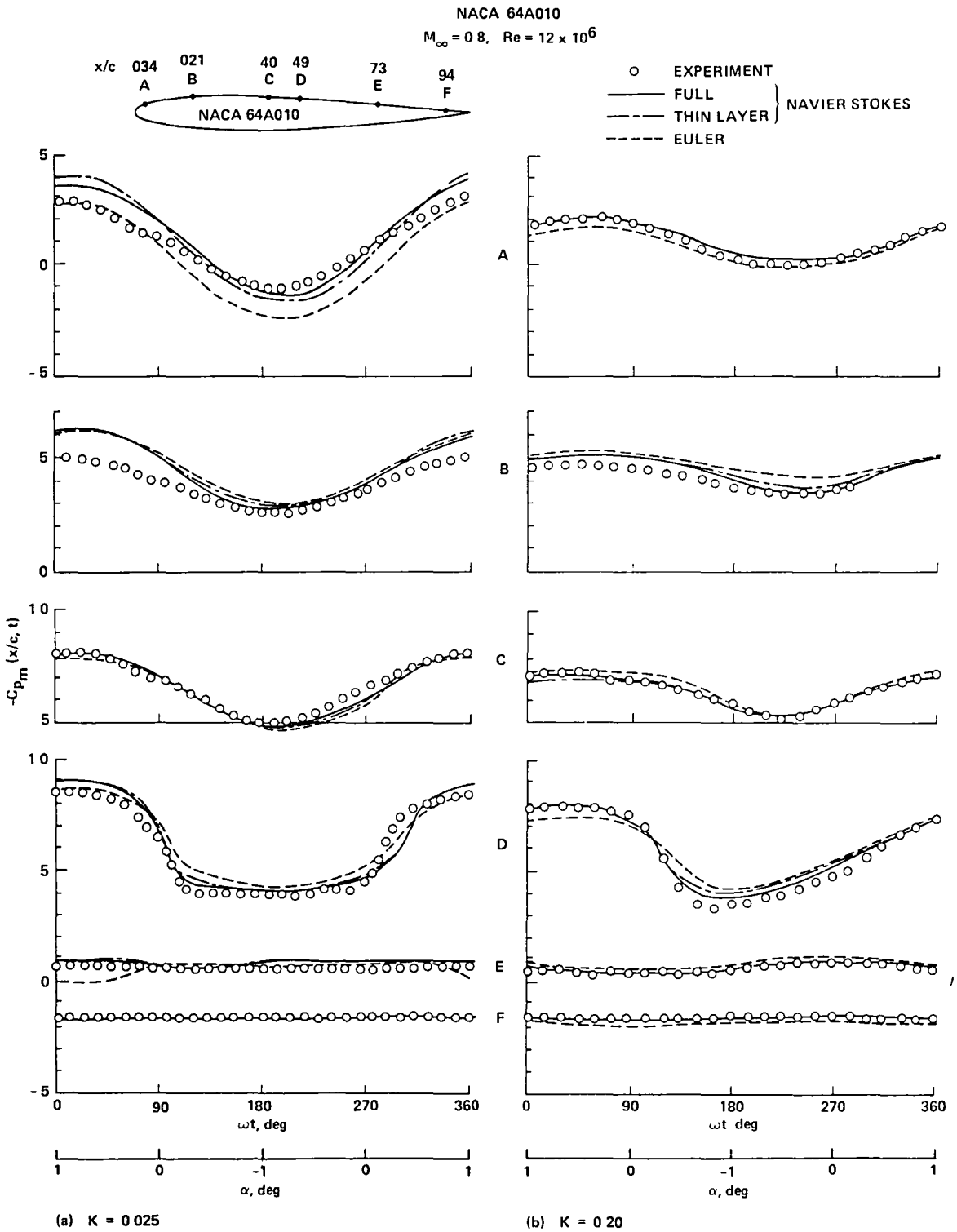

Figure 4 Time-histories of upper-surface pressures NACA 64A010, $\alpha = 0° + 1° \cos \omega t$.

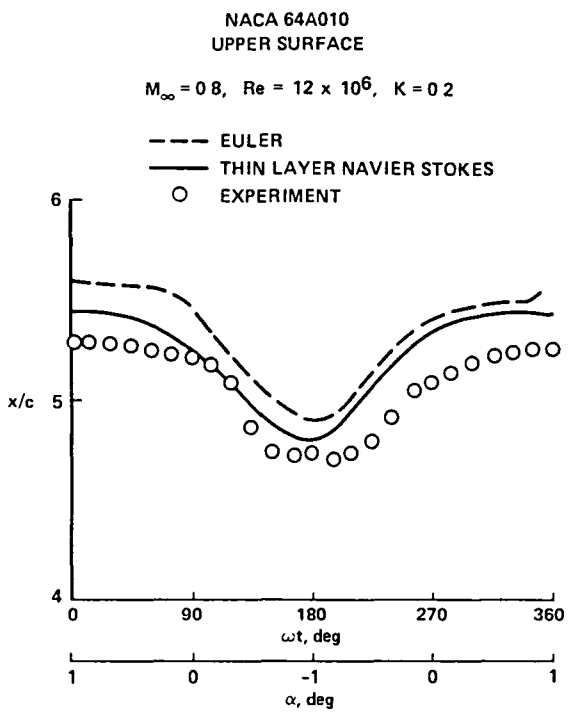

Fig 5 Shock-wave locus on upper surface of the airfoil, $\alpha = 0° + 1° \cos \omega t$.

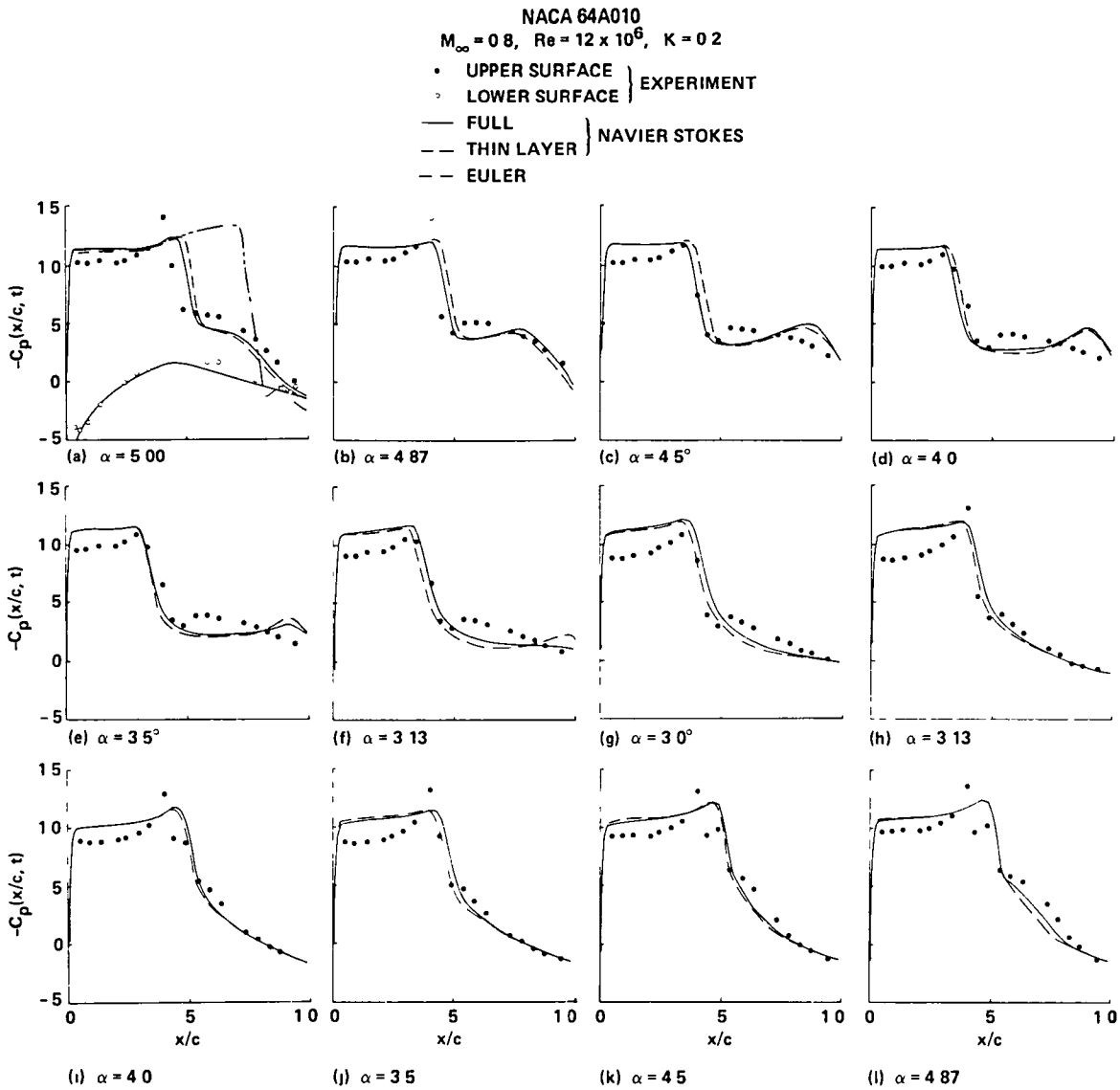

Fig 6. Surface-pressure variation with angle of attack, $\alpha = 4° + 1° \cos \omega t$.

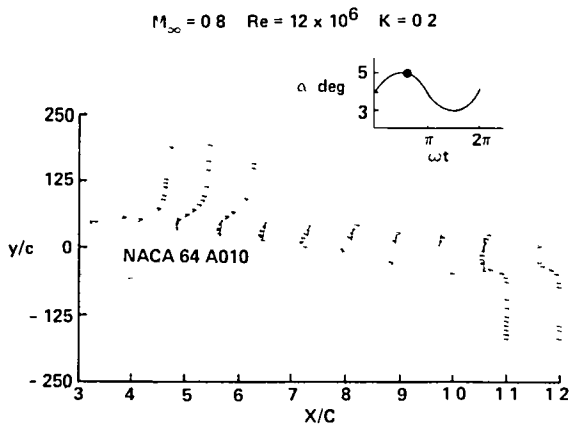

Fig. 7. Computed instantaneous velocity profiles $\alpha = 4\ 87°$ (α decreasing)

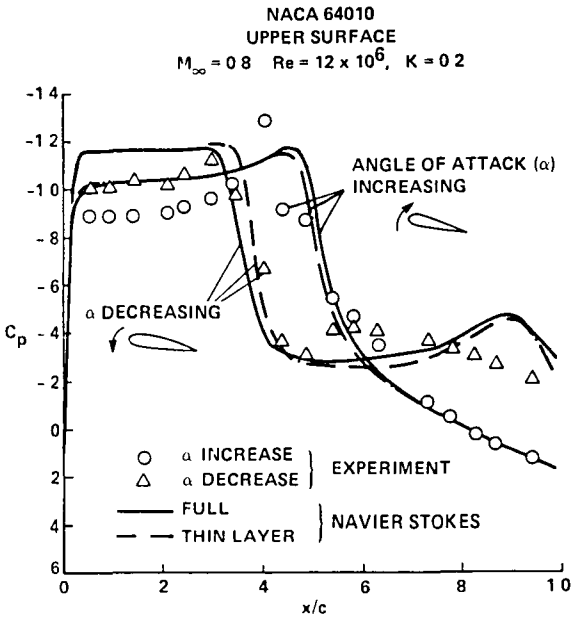

Fig 8. Instantaneous pressures at $\alpha = \alpha_{mean} = 4°$

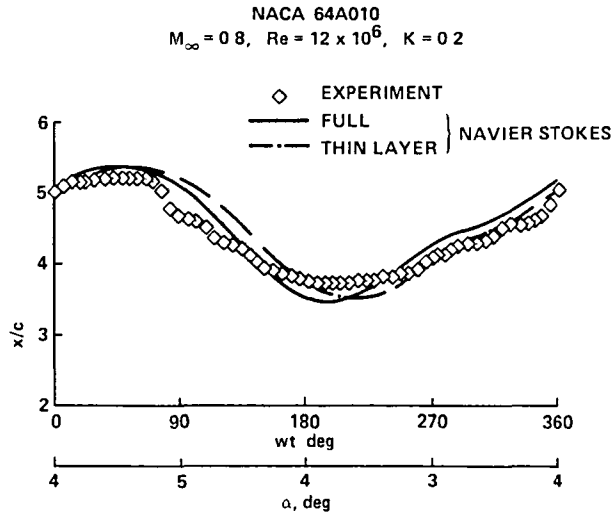

Fig 9 Shock-wave locus on upper surface of the airfoil $\alpha = 4° + 1° \cos \omega t$.

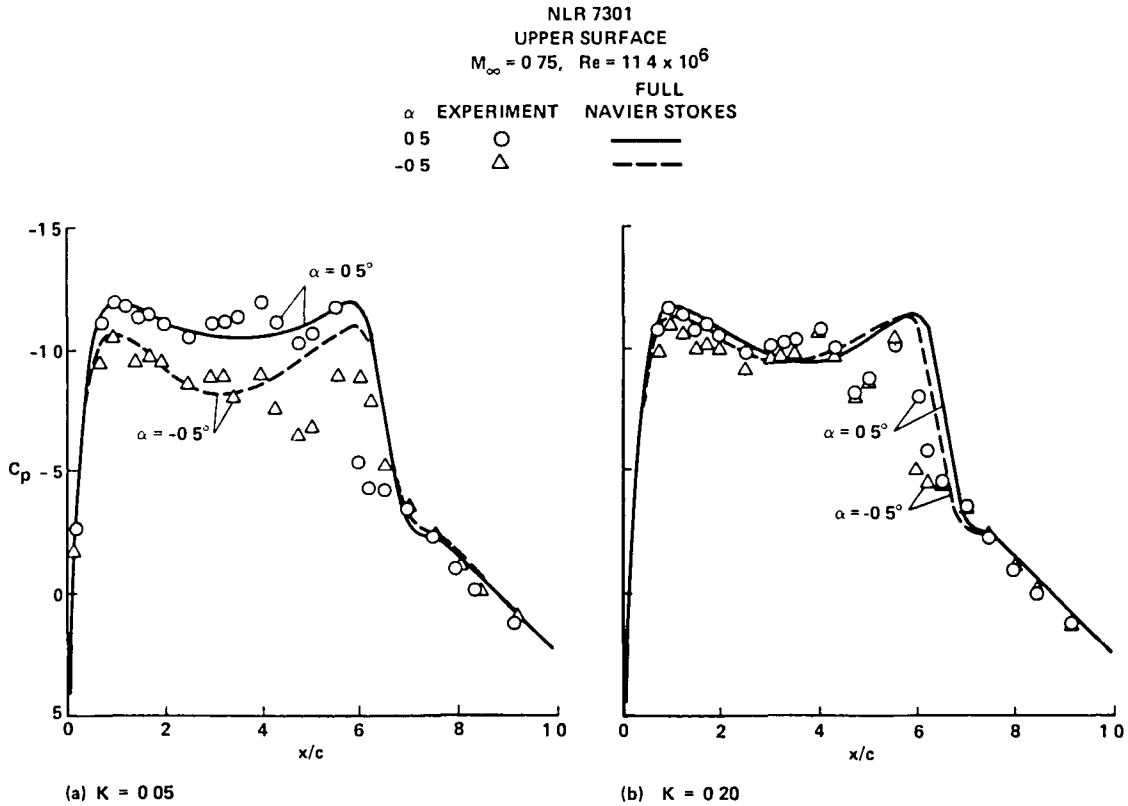

Fig 10. Instantaneous upper-surface pressures at extremes of angle of attack $\alpha = 0.37° + 0.5° \cos \omega t$.

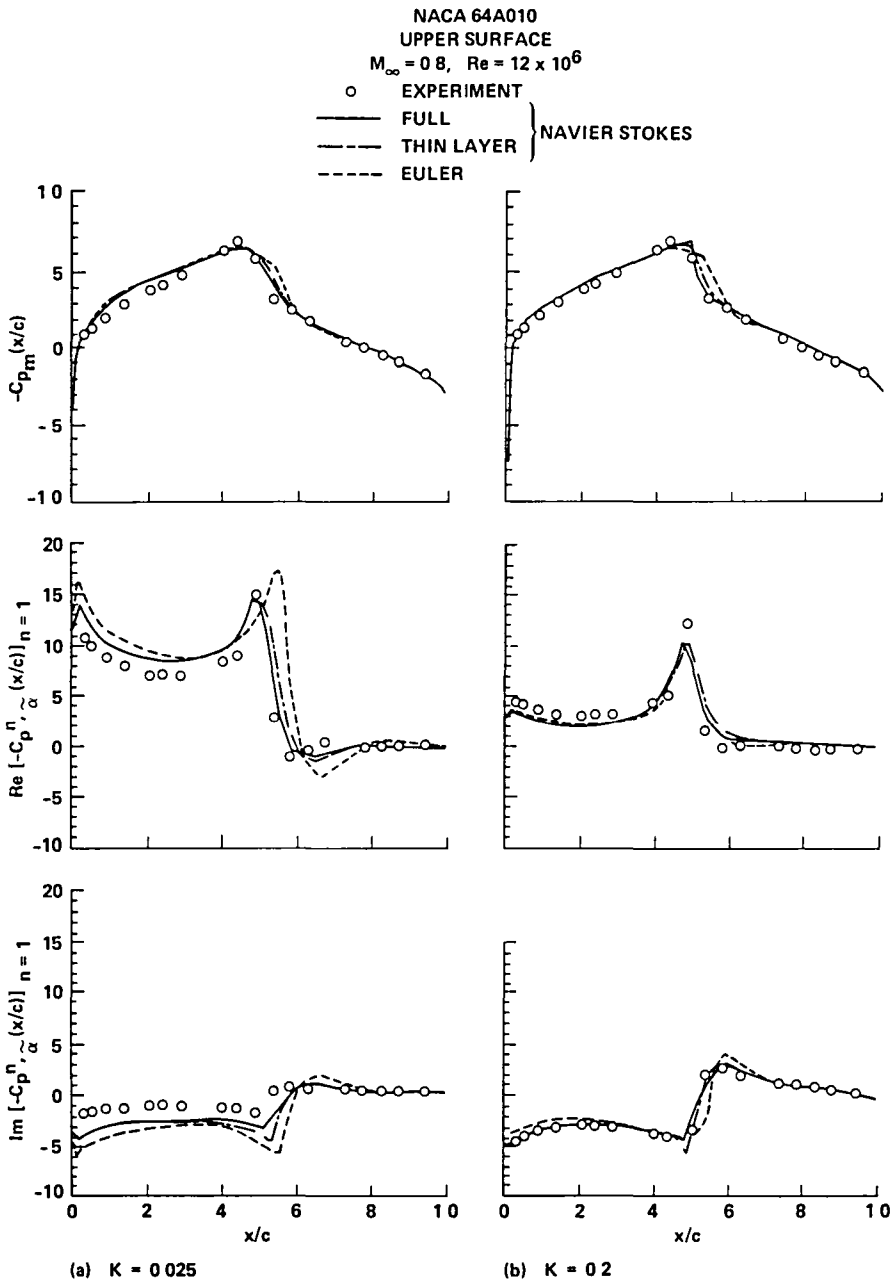

Fig. 11. Mean and first harmonic complex components of pressure coefficients $\alpha = 0° + 1° \cos \omega t$.

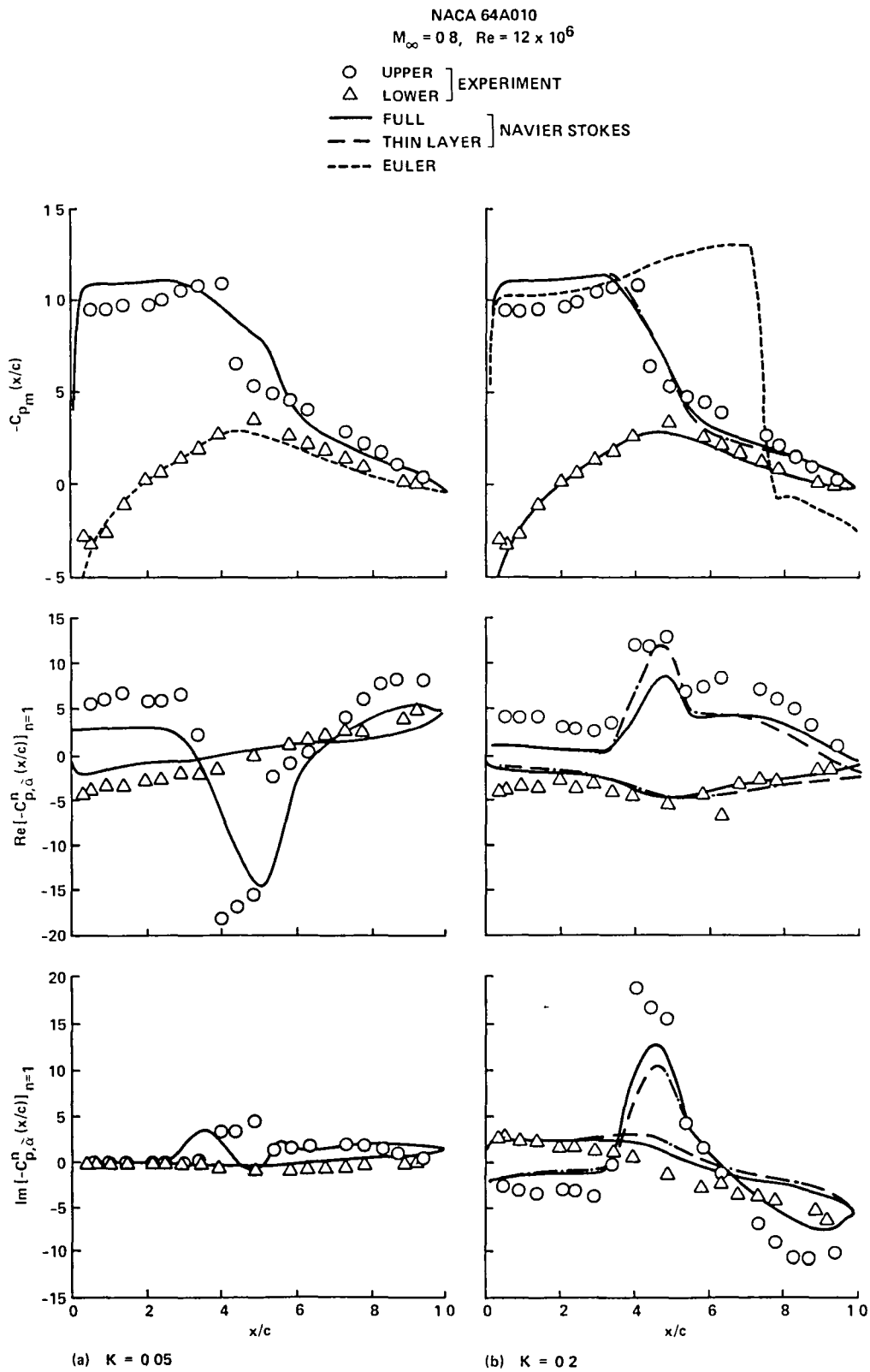

Fig. 12. Mean and first harmonic complex components of pressure coefficients $\alpha = 4° + 1° \cos \omega t$

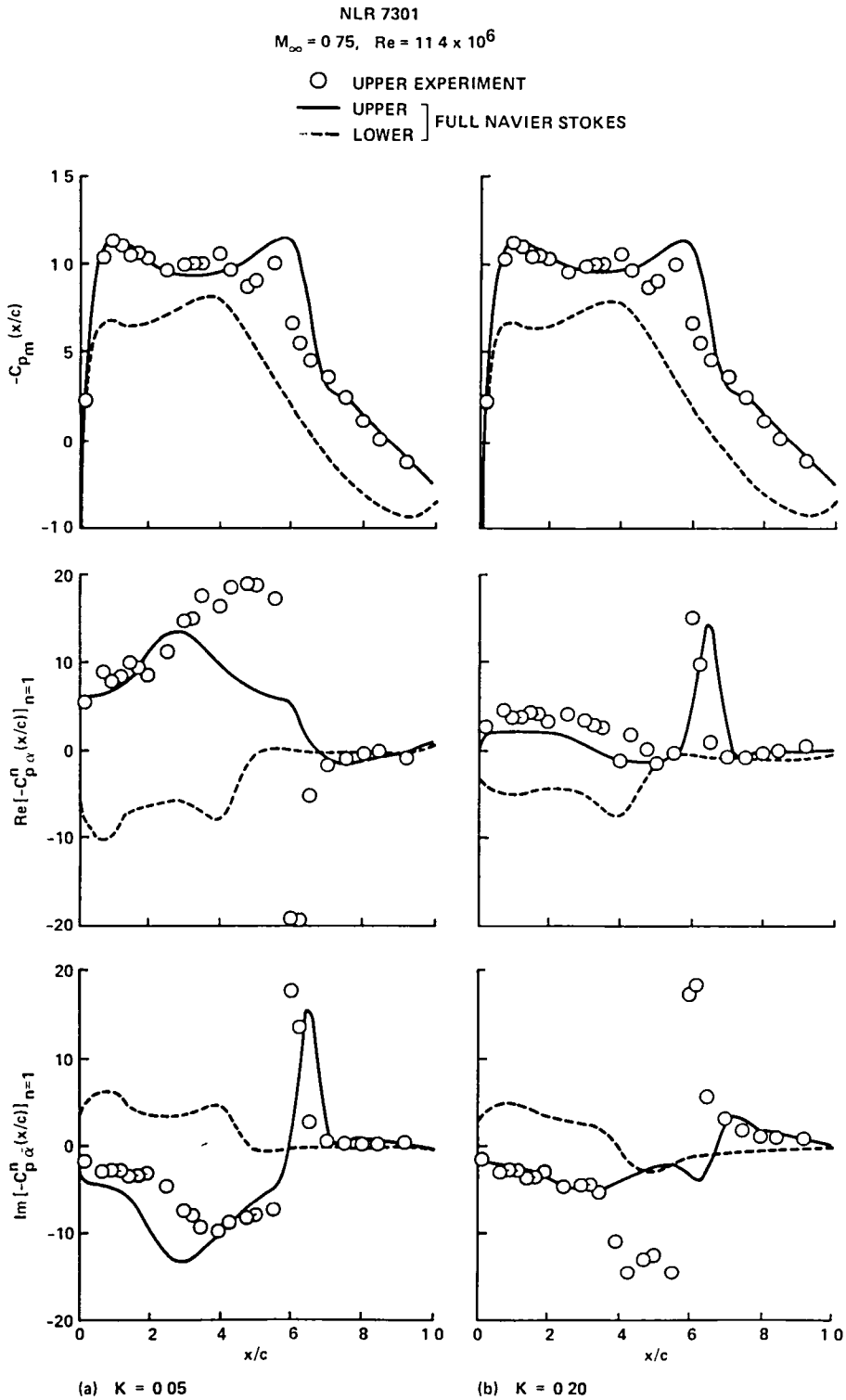

Fig. 13. Mean and first harmonic complex components of pressure coefficients $\alpha = 0.37° + 0.5° \cos \omega t$.

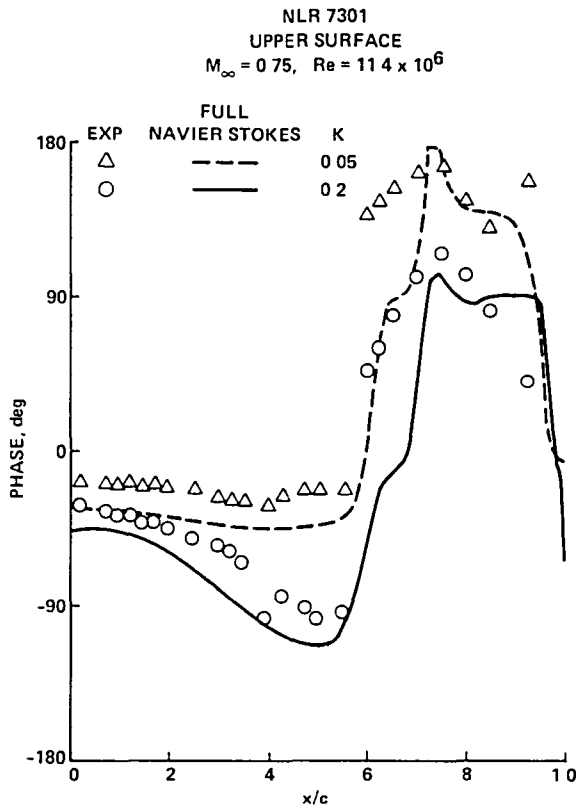

Fig 14 First harmonic phase of surface-pressure variations $\alpha = 0.37° + 0\ 5° \cos \omega t$.

1 Report No	2 Government Accession No	3 Recipient's Catalog No
NASA TM-86011		

4 Title and Subtitle	5 Report Date
NUMERICAL STUDIES OF UNSTEADY TRANSONIC FLOW OVER AN OSCILLATING AIRFOIL	October 1984
	6 Performing Organization Code
7 Author(s)	8 Performing Organization Report No
W. J. Chyu and S. S. Davis	A-9857
9 Performing Organization Name and Address	10 Work Unit No
Ames Research Center Moffett Field, CA 94035	11 Contract or Grant No
12 Sponsoring Agency Name and Address	13 Type of Report and Period Covered
National Aeronautics and Space Administration Washington, DC 20546	Technical Memorandum
	14 Sponsoring Agency Code
	532-06-11

15 Supplementary Notes

Point of Contact: W. J. Chyu, Ames Research Center, MS 227-8, Moffett Field, CA 94035. (415) 965-5655 or FTS 448-5655.

16 Abstract

A finite-difference solution to the Navier-Stokes equations combined with a time-varying grid-generation technique was used to compute unsteady transonic flow over an oscillating airfoil. These computations were compared with experimental data (obtained at Ames Research Center) which form part of the AGARD standard configuration for aeroelastic analysis. A variety of approximations to the full Navier-Stokes equations was used to determine the effect of frequency, shock-wave motion, flow separation, and airfoil geometry on unsteady pressures and overall air loads. Good agreement is shown between experiment and theory with the limiting factor being the lack of a reliable turbulence model for high-Reynolds-number, unsteady transonic flows.

17 Key Words (Suggested by Author(s))	18 Distribution Statement
Unsteady transonic flow Navier-Stokes' equations Supercritical airfoil Oscillative airfoil Computational fluid mechanics	Unlimited Subject Category - 34

19 Security Classif (of this report)	20 Security Classif (of this page)	21 No of Pages	22 Price*
Unclassified	Unclassified	25	A02

*For sale by the National Technical Information Service, Springfield, Virginia 22161

End of Document